RSC Advances

PAPER

View Article Online
View Journal | View Issue

Cite this: *RSC Adv.*, 2019, **9**, 34144

Gold nanostructures for the sensing of pH using a smartphone†

Subrata Biswas,[a] Jayjeet Chakraborty,[b] Avinash Agarwal[b] and Pathik Kumbhakar *[a]

Recently, metal nanostructures have been found to be capable of recognizing small changes in their surrounding environment, which can be utilized as significant sensing tools. In this study, we demonstrated colorimetric sensing of pH by gold nanostructures (GNs) using a simple smartphone. An indigenously developed Android app based on the CIELab 1931 analysis, which could run in a smartphone, was used for the precise determination of the pH value of liquid media. The pH value of an unknown solution obtained from the developed Android app was also compared with that obtained from the conventional ratiometric technique and a commercial pH meter. In another endeavor, it was found that the synthesized GNs demonstrated a high energy transfer efficiency from a donor (namely, the rhodamine 6G, (Rh 6G)) dye. This property of the GNs can be utilized further in the future for studying different bimolecular activities within the human body. It was found that the photoluminescence (PL) of Rh 6G was quenched when it was kept in the vicinity of the synthesized GNs, which was explained in terms of the Förster energy transfer mechanism. Thus, the present study will open up a plethora of opportunities for researchers to employ the nanostructures of gold and other metals in developing low-cost and Internet of Things (IoT)-based sensing devices using only a smart phone.

Received 4th September 2019
Accepted 7th October 2019

DOI: 10.1039/c9ra07101f

rsc.li/rsc-advances

Introduction

In the past few decades, with the advancement of surface plasmon-based (SPR) sensing,[1,2] gold nanostructures (GNs) of different shapes and sizes have become an intensive subject of research due to their wealthy SPR properties in the visible region of the spectrum. Due to the wide tunability in the SPR position of the GNs in the visible region of the electromagnetic spectrum, which can simply be achieved by changing their shape and size, their sensitivity to detect small changes in the refractive index (RI) of the surrounding medium can be increased.[3] On the other hand, spherical mono-dispersed GNs, which are generally pink in color, show an SPR absorption band at ~520 nm. However, upon aggregation, due to the change in any property of a dispersive medium (such as pH and temperature), the SPR position of the GNs shifts to a longer wavelength and the solution changes correspondingly from pink to blue-purple. Since the assemblies of GNs are often accompanied by distinct color changes, colorimetric sensors using GNs have been widely explored, which have found application in the detection of pH,[4,5] DNA,[6,7] proteins[8,9] and metallic ions[10,11] and rapid identification of microorganisms.[12] Thus, the synthesis of GNs with pH-responsive optical properties is becoming increasingly important in the fields of ecology, agriculture, industry, food, medicine, and biology. Moreover, the advent of digital photography and smart phones in the last few decades has revolutionized the idea of data capturing and processing. Moreover, digital cameras and smart phones are used for the development of Internet of Things (IoT)-based devices[13,14] in capturing even small changes in color during any physiochemical process. Interestingly, GNs exhibit bright color under excitation due to their large extinction coefficient of localized surface plasmon resonance (LSPR). It has been reported earlier that as the LSPR position is very sensitive to the inter particle distance,[15] aggregation due to changes in pH or presence of certain analytes provides a fast and handy colorimetric sensing tool. Moreover, GNs can be used for the characterization and quantification of different organic and inorganic molecules attached to their surface.[16,17] Fluorescence spectroscopy is used for probing fluorescent molecules attached to the surface of noble metal nanostructures, which relies on the energy transfer mechanism.[16] The energy transfer is very sensitive to the separation between the donor (metal nanostructures) and acceptor fluorophores (dyes), the quantum yield of dye molecules, and the size and shape of metal nanoparticles.[16] Therefore, fluorescent metal nanostructures and organic fluorophore conjugates have been studied extensively not only to increase the sensitivity but also to improve the performance of biosensors.[18] Thus, by tuning the shape and sizes of metal nanostructures one can manipulate fluorescence signals (enhancement,

[a]*Nanoscience Laboratory, Dept. of Physics, National Institute of Technology Durgapur, 713209 West Bengal, India. E-mail: pathik.kumbhakar@phy.nitdgp.ac.in*

[b]*Department of Computer Science and Engineering (CSE), National Institute of Technology Durgapur, 713209 West Bengal, India*

† Electronic supplementary information (ESI) available. See DOI: 10.1039/c9ra07101f

quenching) within near-optical fields and achieve a single-molecule detection limit.[19]

In this work, we synthesized various architectures of GNs and demonstrated rapid, simple and IoT-based calorimetric sensing of pH using a smart phone. The change in color of the samples due to the change in pH (2 to 8) of the solution was digitally captured in a developed Android mobile app and then the images were analysed based on the CIELab 1931 color space to study the perceptual colorimetric sensor performance. The quantitative color difference (ΔE) between the two images taken at different pH was estimated. It was observed that ΔE depends on the shape of the synthesized nanostructures, and in highly acidic medium (pH 2–4), the specimen with spherical GNs showed the highest ΔE value and for highly alkaline medium (pH 10–12), small-sized gold nanorods showed the highest ΔE value. The ratiometric pH sensing in all the samples was also conducted in the same pH range. The absorption spectra of the samples at different pH were deconvoluted in terms of the absorption peak at 540 nm and 600 nm, and the ratiometric plot (I_{540}/I_{600}) was obtained. The experimental points were fitted with a sigmoid curve and the pH of an unknown solution was measured using calorimetric as well as ratiometric methods, which were found to match quite well with each other. Since the present method for detecting the pH of a solution does not require any sophisticated instruments, it has potential application in field jobs in remote areas where pH detection can be done by using only a smart phone.

In the present study, we also studied energy transfer process between hybrid assemblies of Rh-6G with different shaped GNs. The shape of the GNs was judiciously tuned so that the overlapping integral (J) of the absorption spectrum of GNs with the emission spectrum of Rh-6G changes considerably with changes in shape and size. In all cases of hybrid assemblies of GNs with Rh-6G starting from spherical to rod-shaped particles, quenching of the PL emission intensity with an increase in the concentration of GNs was observed. For the rod-shaped GNs, J was found to be the highest (3.42×10^{16} M^{-1} cm^{-1} nm^4) with the energy transfer efficiency (E) as high as 79.3%. However, for the small spherical GNs, $J = 5.62 \times 10^{14}$ M^{-1} cm^{-1} nm^4 with $E = 44.2\%$. Thus, the hybrid assemblies of Rh-6G with different shaped GNs provide new insight in the energy transfer mechanism when luminescent fluoroprobes interact with different shaped GNs.

Materials and methods

Reagents and materials

Chloroauric acid ($HAuCl_4$, $2H_2O$), silver nitrate ($AgNO_3$), cetyltrimethylammonium bromide (CTAB), ascorbic acid ($C_6H_8O_6$), Rhodamine 6G ($C_{28}H_{31}N_2O_3C$), sodium borohydride ($NaBH_4$), ethanol, sodium citrate, sodium hydroxide (NaOH), and hydrochloric acid (HCl) were purchased from Sigma Aldrich. Glassware was washed with detergent and then sonicated in acetone and Milli Q water prior to use.

Apparatus

For structural characterization, transmission electron microscopy (TEM) images were recorded on a JEOL, JEM 1400plus (JEOL, Japan) operated at 120 kV. UV-Vis absorption spectroscopy measurement of the synthesized gold nanostructures was performed using a UV 1080 instrument (Hitachi, Japan). PL emission spectra of Rh-6G during FRET (Förster resonance energy transfer) analysis were measured on an LS 55 (PerkinElmer). Digital images of the color change during synthesis and pH change were taken using a digital camera (Nikon Coolpix 3600). X-ray crystallographic measurement was performed on a Bruker AXS.

Synthesis of gold nanostructures

The synthesis of gold nanostructures of different shapes involved a two-step process. (i) Firstly, we prepared gold seeds (GNs with a size distribution of 5–10 nm). In a typical procedure, 10 mL 0.2 M solution was prepared and then it was added to 10 mL 0.05 mM solution of $HAuCl_4$ under vigorous magnetic stirring. Then 1.2 mL of ice-cold $NaBH_4$ solution was added to the above solution and an instant color change from yellow to brownish-yellow was observed, indicating the formation of gold seeds in the solution. This solution was left undisturbed for 2 h prior to use.

In the second step, (ii) 50 mL 0.2 M CTAB solution was prepared in four different beakers and under constant stirring 0.5 mL, and 1 mL, 1.5 mL and 2 mL solution of 0.04 M $AgNO_3$ was added to the four different beakers separately, which were marked as S1, S2, S3 and S4, respectively. Subsequently, 50 mL 0.001 M $HAuCl_4$ solution was added to the above growth solution and during the gentle mixing process, 0.7 mL of 0.08 M ascorbic acid solution was added to each of the growth solutions. After 1 min of gentle mixing, 1.2 mL of the seed solution prepared in the first step was added to the above solution and an instant distinct color change in each of the solutions indicated the formation of gold nanostructures of different shapes and sizes.

Assembly of gold nanostructures with Rh-6G

Before preparing the GNs Rh-6G hybrid, CTAB-capped synthesized GNs were extracted several times with a mixed solution of ethanol and hydrochloric acid (36–38%) in a volume mixture of 75 : 1 to remove CTAB from the gold surfaces. Subsequently, the specimen was centrifuged at 10 000 rpm and the collected precipitate was re-dispersed in a 5 μM solution of sodium citrate. Then in a typical set, a fraction of GNs (S0 to S4) from the above solution in varied concentrations ranging from 1–12 μM was added to Rh-6G (0.4 μM), and the final volume was adjusted to 6 mL. After adjusting the pH of the solution to 7, the solution was incubated overnight. The fluorescence spectra of the all the hybrid solutions were measured on a spectrofluorimeter for the FRET analysis.

Colorimetric assay for pH sensing based on aggregation of gold nanostructures

5 mL solution of GNs (S0–S4) with a concentration 0.4 μM was prepared in a test tube. The pH of the solutions was adjusted in the range of 2 to 12 using 1 M HCL and 1 M NaOH and digital photograph of the solution was taken using a digital camera.

UV-Vis absorption spectra were also measured for the flocculation measurements.

Results and discussion

The specimen names (*i.e.* S0–S4) of the synthesized GNs are given according to the protocol discussed in the Experimental section. The UV-Vis absorption spectra of the as-synthesized GNs are presented in Fig. 1a–e, in which the solid black line shows the absorption spectrum of gold seeds (S0), showing the presence of an absorption band at ~500 nm. The absorption peak is not very distinct for the gold seeds because they were very small in size, as can be seen in the TEM images provided in the adjacent right panel. However, in the case of S1, in which the formation of spherical GNs occurred, a clear absorption peak at ~534 nm was observed due to surface plasmon resonance (SPR). In the case of S2, the SPR absorption peak was red-shifted, giving a clear indication of the anisotropic growth[20] of GNs, which is also evident in the corresponding (representative) TEM image showing the formation of some rice-like structures.

The absorption spectra of S3 and S4 are found to consist of two SPR peaks, one at ~527 nm and the other at a longer wavelength of ~591 nm for S3, which is shifted further to 598 nm for S4. The linear optical absorption properties of the anisotropic-shaped metal nanoparticles, which arise due to different higher order multipolar plasmon resonances, have been studied theoretically and experimentally earlier by various researchers in great detail.[21–24] However, the plasmon oscillation at the shorter wavelength region observed in S3 and S4 of this work is due to quadrupole resonance.[21] On the other hand, the plasmon absorption band observed at the higher wavelength is due to the dipole resonance.[21] The dipole resonance is more sensitive than the quadrupolar resonance in response to environmental changes, such as shape and size of GNs, refractive index (RI) of the surrounding medium and attachment of any ligands.[22–24] The digital photographs of the specimens, taken under visible light illumination, are shown in the adjacent vertical panel (right hand side) of Fig. 1a–e, which show the color of the specimens.

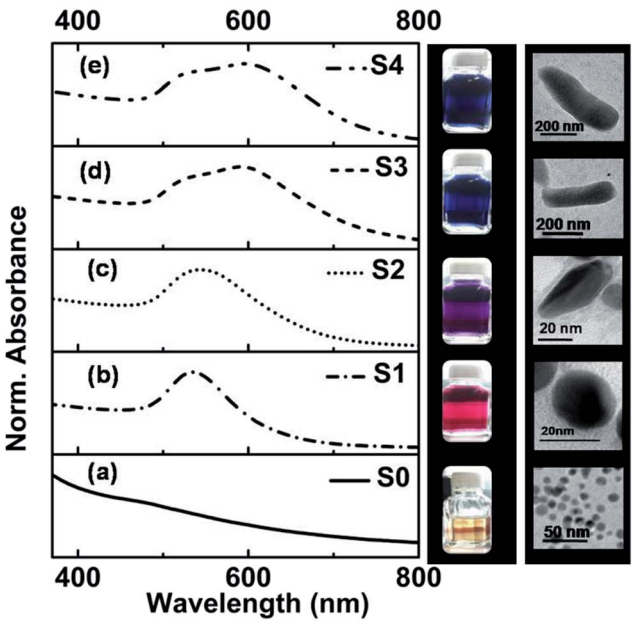

Fig. 1 (a–e) UV-Vis absorption spectra of gold seeds (S0) and the different GNs (S1–S4). The corresponding digital photograph image (color) under visible light illumination and the typical TEM images of the specimens are shown in the adjacent vertical panel (right hand side).

The phase and crystallinity of the samples were investigated *via* the X-ray diffraction (XRD) technique, and the XRD patterns of S0 and S1 are shown in Fig. S1.† Three distinct peaks at $2\theta = 38.1^\circ$, 44.3° and 64.5° corresponding to the crystallographic planes of (111), (200) and (220), respectively,[25] appeared in the XRD pattern. It was found that the intensity of the diffraction peaks for S1 was much higher than that of S0, *e.g.* the (111) peak of S1 was 2.5 times more intense than that of S0. The TEM images of S0, which is termed seed, show that it consists of spherical nanostructures with an average particle size of 8 ± 2.2 nm. The TEM image of S1 shows that its particles are spherical in shape, but their size increased to 20 ± 4 nm. As we discussed earlier, we used different concentrations of $AgNO_3$ for the synthesis of different nanostructures of Au and the concentration of Ag^+ ions plays a crucial role in determining the final shape of GNs.[26,27] It was found that there was an evolution of the shape of the anisotropic-shaped nanostructures of Au. It was found from the TEM images, as shown in the right panel of Fig. 1e, that S2 consists of nanorice- or cylindrical-shaped particles, S3 consists of nanorods and S4 consists of nanorods having a typical length as long as ~1 μm. This shape anisotropy can be attributed to the formation of Ag–Br complex assemblies in the presence of CTAB, which acts as a face-specific capping agent and promotes the growth in some specific direction.[28,29] It has also been shown earlier that the presence of Ag and Br may modulate the self-templating effect of CTAB micelles, and thus the transition from spherical to cylindrical shapes has also been reported earlier.[30] The possibilities of the potential deposition of a sub-monolayer of Ag on the lateral gold nanorods in our case of S3 and S4 specimens were ruled out since the pH of the solution during the synthesis was 6, and thus the possibility of the reduction of Ag^+ to Ag^0 by ascorbic acid was not possible.[31]

Ratiometric absorption-based gold nanosensors[32,33] have been developed by earlier researchers for the sensing and quantification of pH. In our case, it was found that a small change in pH led to the agglomeration of GNs, resulting in a corresponding change in the UV-Vis absorption spectra and color of the specimens under visible light illumination. Thus, by monitoring the UV-Vis absorption spectra of GNs dispersed in different pH environment, it is possible to sense the pH of the environment. The UV-Vis absorption spectra of GNs were also monitored while varying the pH of the sols in the wide range of pH 2 to 12 (shown in Fig. S2a–d of ESI†). The pH of the gold sol was changed here using HCl and NaOH.

The titration curves[34] for all the samples were plotted by deconvolution of the absorption spectra in terms of the absorption peaks at 540 nm and 600 nm, and the ratiometric absorbance value (I_{540}/I_{600}) *vs.* pH was plotted. The titration curves for S1–S4

specimens are depicted in Fig. 2a–d, respectively, in which the scattered points are the experimental data and the solid lines are the corresponding sigmoid fitting. Also, the integrated absorption data covering the 600–800 nm region was evaluated to explore the extent of the agglomeration (flocculation)[35] of the nanostructures with a change in the pH of the solution, and the results are plotted in Fig. 2e–h. The experimental points were fitted with a sigmoid curve, which showed a smother variation with a change in pH in comparison to the ratiometric plot. We also utilized the ratiometric plots and sigmoid fitting in both cases for the determination of unknown pH. The discussion on the determination of unknown pH is given later at the end of the Results and discussion section.

However, the method of sensing pH using the ratiometric plot is not robust and requires a sophisticated spectrometer. Thus, the measurement of pH in remote areas where lab facilities are not close, is practically beyond the reach of common people. On the other hand, after the introduction of smartphones and their widespread reach to common people, it is becoming cost effective, portable, and easy to use digital platforms. Therefore, we explored herein, an ingenious approach of using a smart phone for sensing pH using the synthesized GNs, and the results are discussed below.

The digital photographs of the synthesized gold sols dispersed in media with different pH showed prominent changes in color, as depicted in Fig. 2i–l. Based on the digital image and using a smart phone, as shown schematically in Fig. 2m, we evaluated the colorimetric sensing performance of our GNs by mapping the image data to CIELab 1931. One of the major advantages of colorimetric sensing using the CIELab color representation is that it is device-independent, and thus it is possible to compare the photographed images.[36–38] In the CIELab coordinates, any color is represented using tristimulus values, lightness L^* and chromaticity a^* and b^*. Color directions are represented by a^* and b^*, where $+a^*$ is the red axis, $-a'$ is the green axis, $+b^*$ is the yellow axis and $-b^*$ is the blue axis. The lightness dimension, represented by L^*, ranges from 0 (pure black) to 100 (diffuse white). The point at which the a^* and b^* axes cross at the L^* value of 50 is pure, balanced and neutral gray. The RGB (XYZ) values are obtained by using an ingeniously developed app from the digital images of the specimens while keeping them at different pH environment. The CIE tristimulus values X, Y and Z and tristimulus values for illuminant X_n, Y_n and Z_n are related to L^*, a^* and b^* by the following relations if X/X_n, Y/Y_n and Z/Z_n are all greater than 0.008856, respectively.

$$L^* = 116\left(\sqrt[3]{\frac{Y}{Y_n}}\right) - 16 \tag{1a}$$

$$a^* = 500\left(\sqrt[3]{\frac{X}{X_n}} - \sqrt[3]{\frac{Y}{Y_n}}\right) \tag{1b}$$

$$b^* = 200\left(\sqrt[3]{\frac{Y}{Y_n}} - \sqrt[3]{\frac{Z}{Z_n}}\right) \tag{1c}$$

When the values of X/X_n, Y/Y_n and Z/Z_n are found to be equal to or less than 0.008856 the following relations are used.

$$L^* = 903.3\left(\frac{Y}{Y_n}\right) \tag{1d}$$

$$a^* = 500\left[7.87\left(\frac{X}{X_n}\right) - 7.87\left(\frac{Y}{Y_n}\right)\right] \tag{1e}$$

$$b^* = 200\left[7.87\left(\frac{Y}{Y_n}\right) - 7.87\left(\frac{Z}{Z_n}\right)\right] \tag{1f}$$

In the present case, we used D65 as the standard illuminator, where the CIE tristimulus values, X_n, Y_n and Z_n are taken as 95.02, 100 and 108.82, respectively. Thus, the values of X/X_n, Y/Y_n and Z/Z_n are all greater than 0.008856, and we used eqn 1(a)–(c) to evaluate L^*, a^* and b^*, respectively. The Euclidean distance between the two color points (ΔE)[38,39] in the CIELab color representation is given by the following formula:[38,39]

$$\Delta E = (\Delta L^{*2} + \Delta a^{*2} + \Delta b^{*2})^{1/2} \tag{1g}$$

where ΔL^*, Δa^* and Δb^* are the difference between two color points in lightness L^*, and chromaticity a^* and b^* axes, respectively. Thus, the ΔE value can be used as an indicator to measure the perceived color difference by an observer. It has been reported that the minimum value of ΔE for which the human eye can detect the color difference between two color points is ~1. The Android app, which was ingeniously developed in this work, can capture the digital photograph of the samples and simultaneously determine the pH based on eqn 1(a)–(d). The experimental arrangement to determine the pH value through the Android app is schematically demonstrated

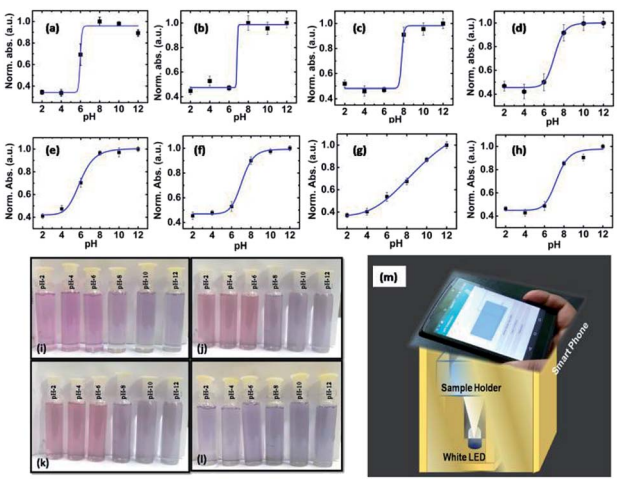

Fig. 2 (a–d) Titration curves for specimens S1–S4 and (e–h) extent of the agglomeration (flocculation) value of the GNs with a change in the pH of the solution, respectively. (i–l) Color of specimens S1 to S4 in different pH environment starting from 2 to 12, respectively. (m) Experimental design to capture a digital photograph of the specimen in different pH environment and simultaneous determination of the pH value by Android application.

in Fig. 2m. The developed Android application can run in offline mode, which indicates its usability in real-life environment. The ΔE value between two color points obtained at different pH was evaluated using the RGB values, and are presented in Table 1. It was observed that the ΔE value in each case for all specimens was well above the perceived color threshold of $\Delta E \sim 1$ by the human eye. The technical details of the development of the Android application are discussed in detail in the ESI, S4.†

The obtained tristimulus values for each specimen in different pH environment are also shown in the chromaticity diagram in Fig. 3a–c. It was found that the tristimulus values rotate in a counterclockwise manner for the specimens S1, S2 and S3, but for specimen S4 it rotates in a clockwise fashion (for S4 specimen shown in Fig. S6†) from the pink to blue region of the chromaticity diagram. Also, it was observed that the tristimulus values for each specimen for different pH are well separated in the chromaticity diagram. The sensitivity of the synthesized materials for pH sensing can be understood further by calculating the inverse of the slope of ΔE *vs.* pH curve. The ΔE *vs.* pH curves for S1 to S4 are presented in Fig. 3d and the results are summarized in Table 1. From Table 1, it can be observed that the sensitivity (ΔpH/ΔE) of samples S1–S3 is much higher than that of S4 in acidic and basic media. The accuracy of the used colorimetric sensing technique was evaluated further by measuring the unknown pH using the same GNs and then the results were compared with that obtained *via* the conventional ratiometric sensing technique and also with the experimental values obtained directly from a commercial digital pH meter. For this, we dispersed the specimen in a solution with unknown pH and digital photographs (shown in the Fig. S7a†) were taken under the same experimental conditions, and the unknown pH was evaluated for each specimen using the same Android app.

The determination of unknown pH using the ratiometric technique was done by measuring the absorption spectrum (shown in Fig. S7b†) of the specimen in the unknown pH solution. Then the absorption spectrum was deconvoluted and the corresponding flocculation value was determined for each sample. Thereafter, using the fitting presented in Fig. 2e–h, we determined the pH of the unknown solution. Finally, we used a pH meter to determine the pH of the unknown solution, and all the results are summarized in Table 2. It is evident from Table 2 that the results obtained from the colorimetric sensing technique using the Android app are very close to that obtained from the commercial pH meter and ratiometric sensing techniques.

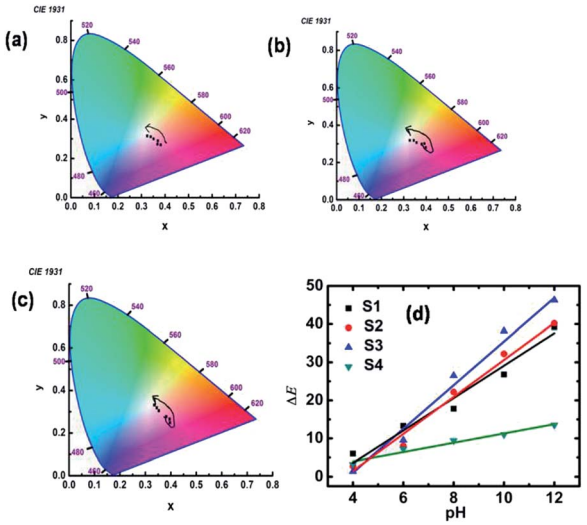

Fig. 3 (a–c) Tristimulus values for S1 to S3 in different pH environment in the chromaticity diagram, respectively. (d) Variation in ΔE with pH for specimens S1, S2, S3 and S4.

Also, for the determination of the pH of some real-life samples, we collected rainwater, water from a municipality supply line and roadside drinking beverages as our test samples. Firstly, we determined the pH of the real-life sample using a commercial pH meter and then with our ingeniously developed smart phone-based app. The pH of the drinking beverages, rainwater and water from the municipality supply line was found to be 3.7, 5.9 and 7.2, respectively, as determined by the commercial pH meter. The pH of these sample was also determined using digital photographs using our ingeniously developed smartphone app, which was found to be 3.65 ± 0.29, 6.12 ± 0.32 and 7.18 ± 0.56, respectively. Therefore, the obtained results show excellent agreement with the pH value determined by the commercial pH meter and that obtained from the developed smartphone-based app.

Hence, it can be concluded from this study that the synthesized GNs can be suitably used in pH sensing just by employing an Android phone, and may find application in IoT-based devices for use in remote places, where the installation and transportation of different experimental instruments are truly challenging.

It is well-known that the Förster resonance energy transfer (FRET) is a powerful technique for probing small changes in separation distance between donor and acceptor fluorophores,

Table 1 The results from the measurement of ΔE value at different pH

	Standardized indicator for the perceived color difference by an observer (ΔE)				
Specimen	pH = 2–4	pH = 4–6	pH = 6–8	pH = 8–10	pH = 10–12
S1	6.08	13.32	15.95	25.09	42.7
S2	2.78	8.07	22.22	32.23	40.8
S3	1.36	9.54	26.53	38.21	44.3
S4	3.42	7.27	9.47	11.09	13.5

Table 2 The results from the measurement of unknown pH using colorimetric and ratiometric techniques and a commercial pH meter

Method	S1	S2	S3	S4
Colorimetric	9.9 ± 0.24	9.8 ± 0.16	10.2 ± 0.34	10.1 ± 0.12
Ratiometric	9.8	10.1	9.9	9.8
Commercial pH meter	9.8	9.8	9.8	9.8

leading to applications in sensing.[43–49] In the present case, Rh-6G was used as a fluorescence probe to study the change in its emission behavior in the presence of GNs of different shape and sizes. Rh-6G is a cationic dye belonging to the family of Xanthene dyes[40] and it shows high photostability, high quantum yield, is less prone to photobleaching[41] and provides emission and absorption in the long visible wavelength region, which enhance its probability to have spectral overlap between its absorption spectrum and the emission spectrum of GNs. Thus, Rh-6G has been widely used as a fluorescence probe to study different energy transfer processes such as FRET,[42] RET (resonance energy transfer)[43] and MEF (metal enhance fluorescence).[44]

Fig. 4a presents the absorption (black solid line) and emission spectra (blue dotted line) of S4 and Rh-6G together after dispersing them in aqueous medium. The absorption band is found to extend from 450 nm to 600 nm, with a peak at 526 nm which corresponds to the free monomeric absorption of Rh-6G. A shoulder peak appeared between 475–500 nm, which corresponds to the absorption of the H form of the Rh-6G dimer.[45] Since the intensity corresponding to the 526 nm absorption peak is much higher than that of the shoulder peak, we can conclude that the monomeric form of Rh-6G existed in the used concentration of Rh-6G. The emission spectrum of Rh-6G, recorded at an excitation wavelength of 525 nm showed a peak at 560 nm, as presented by the blue dotted line in Fig. 4a.

The inset of Fig. 4b shows a schematic of the possible interaction pathway between Rh-6G and trisodium citrate (TSC)-stabilized GNs. Since Rh-6G is a cationic dye, here we used the ion exchange process (details given in the Materials and Synthesis section) to replace CTAB with TSC, which is an anionic stabilizing agent.[46] It was found that the absorption spectrum of S4 has considerable overlap with the emission spectrum of Rh-6G, as shown in Fig. 4a, confirming the finite possibility of energy exchange between GNs and Rh-6G. Fig. 4c presents the PL emission spectra of Rh-6G (0.4 μM) in the presence of S4 with an increase in concentration from 0–12 μM. However, for the S0–S3 specimens, the static PL emission spectra are presented in the ESI (Fig. S9a–d†). In all cases, we observed that quenching of the PL emission intensity occurred with an increase in the concentration of GNs, but it was found that the quenching efficiency varied widely when the experiment was carried out with different shaped GNs. Fig. 4d shows the ratio of the PL emission intensity of Rh-6G in the absence and presence of GNs. In Fig. 4d, the scattered points are the experimental points, which were fitted (solid lines) with the Stern–Volmer equation to extract the Stern−Volmer constant (K_{SV})[47] given by the following equation:

$$F_0/F = 1 + K_{SV} \times C \quad (2)$$

where F_0 (F) is the fluorescence intensity in the absence (presence) of GNs and C is the concentration of GNs. The extracted values of K_{SV} for all the specimens are given in Table 3.

The observed quenching of the PL emission intensity of dye molecules is attributed to the non-radiative energy exchange process[48] between the dye molecules and metal nanostructures. This type of energy exchange process can be explained in terms of dipole–dipole interaction between molecular fields of donor–acceptor and gives an energy exchange probability, which is greater than its molecular diameter called the Förster radius and is given by:[49]

$$R_0 = [(9 \ln(10)\, k^2 \varphi J)/(128\pi^2 N_A n^2)]^{1/2} \quad (3)$$

where R_0 is the Förster radius, $k = 2/3$, φ is the fluorescence quantum yield, J is the overlapping integral, N_A is the Avogadro number, and n is the refractive index of the solvent. The Förster energy transfer process is generally limited up to a distance of 80 Å between a donor–acceptor pair. However, for metal nanostructures, due the strong local field originating from SPR in the visible region, the energy exchange with fluorophores is possible even at a large distance of up to 700 Å.[50] Together with the above factors, the shape of metal nanostructures may contribute to the non-radiative energy transfer processes. Since the local plasmonic field depends on the

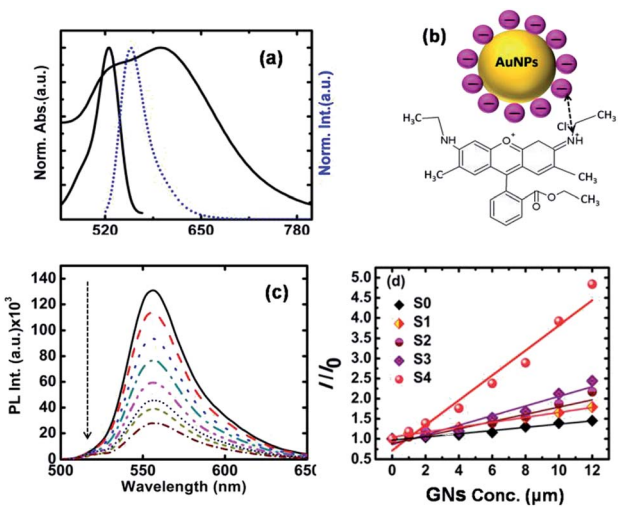

Fig. 4 (a) Absorption spectra of Rh-6G and S4 specimen (black solid line) and emission spectrum of Rh-6G (blue dotted line) in aqueous medium. (b) Schematic of the possible interaction pathway between Rh-6G and TSC-stabilized GNs. (c) PL emission spectra of Rh-6G (0.4 μM) in the presence of S4 specimen with an increase in the concentration of GNs from 0–12 μM. (d) Plot of the intensity ratio of the PL emission spectra of Rh-6G after and before the addition of GNs, where the scattered points are the experimental points and the solid line is the Stern–Volmer fitting.

Table 3 The calculated values of J (M^{-1} cm^{-1} nm^4), K_{SV} (M^{-1}), E, R_0 (Å) and r (Å)

Specimen	J (M^{-1} cm^{-1} nm^4)	K_{SV} (M^{-1})	E	R_0 (Å)	r (Å)
S0	2.57×10^{13}	4×10^4	32.1	24.2	27.4
S1	5.62×10^{14}	6×10^4	44.2	40.6	42.2
S2	2.98×10^{15}	9×10^4	54.1	53.3	51.8
S3	1.42×10^{16}	1.2×10^5	64.3	69.5	63.1
S4	3.42×10^{16}	3×10^5	79.3	139.3	111.6

shape of the nanostructures, there is a large local field enhancement in the case of anisotropic metal nanostructures such as triangular-, rice- and rod-shaped particles at their sharp corners. In the present case, the shape anisotropy increased going from S0 to S4, and thus the highest quenching efficiency was observed in S4. Another important fact is that the overlapping integral J, which measures the overlapping of the absorption spectrum of the acceptor (metal nanoparticle) and emission spectrum of the donor (Rh-6G), was found to increase as the shape anisotropy increase. This also explains the reason for the occurrence of the best quenching efficiency in S4 among the specimens. We also measured the absorption spectra of all the GNs with an increase in the concentration of Rh-6G, and the absorption spectra of S1 and S4, are provided in the ESI (Fig. S10a and b†). In all cases, we observed a very negligible red shift in the absorption peak together with a slight decrease in the absorbance of Rh-6G dye up to a certain concentration of 4 μM of GNs, which clearly indicate the very feeble electron transfer probability from Rh-6G to the metal nanostructures and quenching of the fluorescence intensity is mainly dominated by a Förster-type energy transfer process. However, for the S4 specimen, above a concentration of 4 μM GNs, there is a detectable shift in the absorption peak and a decrease in absorbance is observed. Thus, for the S4 specimen together with Förster-type energy transfer, some nonradiative electron transfer may be occurring. The Förster energy transfer rate ($K_F(r)$) was evaluated for a given distance r between the donor–acceptor molecule for each sample using the relation[50]

$$K_F(r) = \{\varphi \times k^2 \times 9000 \times \ln(10) \times J\}/ \{\tau_D \times r^6 \times 128 \times \pi^2 \times N_A \times n^4\} \quad (4)$$

where τ_D is the fluorescence lifetime of the donor molecule and r is the distance between the acceptor and donor. The energy transfer efficiency (E) can also be evaluated by using the relation

$$E = (1 - F/F_0). \quad (5)$$

The energy transfer efficiency can also be described as $E = (r^6)/(r^6 + R_0{}^6)$, where once R_0 is known using eqn (3) and E using eqn (5), we can easily determine r, which is the distance between the donor–acceptor pair. All these parameters for the resonance energy transfer were evaluated and summarized in Table 3. It is evident from Table 3 that the distance between the metal nanoparticle and Rh-6G in the case of S4 specimen crossed the usual FRET-type energy transfer processes, as discussed earlier. However, the value of J is quite high in the case of S4. Thus, resonance energy transfer may be the possible mechanism for the energy transfer in this case. Also, cationic dyes such as Rh-6G may bind preferentially with the particular surface of the citrate-stabilized rod-shaped gold nanostructures of several nanometers in length, and thus we observed the best quenching efficiency for S4. Thus, the synthesized gold nanostructures may be used as a plasmonic ruler to monitor *in vivo* energy transfer processes at large distances and may overcome the limitation of the usual FRET-type energy transfer process.

Conclusions

In the present study, we exploited the visible color change of GNs with a change in the pH of the surrounding medium (2–12) due to the agglomeration of GNs to demonstrate the smart phone-based colorimetric sensing of pH. An ingeniously developed handset independent Android application based on CIELab 1931 analysis was used for the precise determination of the pH value. The conventional ratiometric technique and a commercial pH meter were also used for the authentication of the pH value obtained from the Android app for the unknown pH of a solution. It is noteworthy to mention that the pH value obtained from the Android app remarkably matched the pH value obtained from the ratiometric technique and commercial pH meter. We also investigated the energy transfer process between different shaped GNs with Rh-6G, and observed that with an increase in the value of the overlapping integral between the absorption spectrum of the acceptor (gold nanostructures) and fluorescence spectrum of the donor (Rh-6G), the energy transfer efficiency reaches the maximum, and we observed almost 80% PL quenching in the case of specimen S4. Thus, the synthesized GNs also can be used as a bimolecular sensing platform within the human body since energy exchange is very sensitive to any physiochemical change in the vicinity of the donor acceptor pair. Therefore, the synthesized GNs may find broad IOT-based sensing applications, which require only a smartphone and will provide better portability and sensitivity as a low cost sensing tool.

Conflicts of interest

There is no conflicts of interest.

Acknowledgements

Authors are thankful to Dept. of Science & Biotechnology, Govt. of W. B., Kolkata, for the project grant no. 332 (Sanc.)/ST/P/S&T/16G-24/2018 dt. 06.03.2019. Also authors are thankful NIT Durgapur, Ministry of Human Resource Development, Government of India, and Technical Education Quality Improvement Program (TEQIP–III), Govt. of India for the partial supports.

References

1 H. B. Jeon, P. V. Tsalu and J. W. Ha, *Sci. Rep.*, 2019, **9**, 13635–13642.
2 K. M. Maye and J. H. Hafner, *Chem. Rev.*, 2011, **111**, 3828–3857.
3 Z. Yong, D. Y. Lei, C. H. Lam and Y. Wang, *Nanoscale Res. Lett.*, 2014, **9**, 187–193.
4 S. Jung, J. Nam, S. Hwang, J. Park, J. Hur, K. Im, K. Park and S. Kim, *Anal. Chem.*, 2013, **85**, 7674–7681.
5 L. S. Lawson, J. W. Chanac and T. Huser, *Nanoscale*, 2014, **6**, 7971–7980.
6 (*a*) J. Zhang, S. Song, L. Wang, D. Pan and C. Fa, *Nat. Protoc.*, 2007, **2**, 2888–2895; (*b*) L. Zou, R. Shen, L. Ling and G. Li, *Anal. Chim. Acta*, 2018, **1038**, 105–111.

7 C. Park, H. Park, H. Jin, L. Hye, S. Lee, K. H. Park, C. Choi and S. Na, *Microchim. Acta*, 2019, **186**, 1–34.
8 M. H. Jazayeri, T. Aghaie, A. Avan, A. Vatankhah and Md. R. S. Ghaffarid, *Sens. Biosensing Res.*, 2018, **20**, 1–8.
9 J. Wu, Y. Qu, Q. Yu and H. Chen, *Mater. Chem. Front.*, 2018, **2**, 2175–2190.
10 V. Poornima, V. Alexandar, S. Iswariya, P. T. Perumal and T. S. Uma, *RSC Adv.*, 2016, **6**, 46711–46722.
11 F. Najafzadeh, F. Ghasemi and M. R. Hormozi-Nezhad, *Sens. Actuators, B*, 2018, **270**, 545–551.
12 B. Li, X. Li, Y. Dong, B. Wang, D. Li, Y. Shi and Y. Wu, *Anal. Chem.*, 2017, **89**(20), 10639–10643.
13 C. Dong, Z. Wang, Y. Zhang, X. Ma, M. Z. Iqbal, L. Miao, Z. Zhou, Z. Shen and A. Wu, *ACS Sens.*, 2017, **2**, 1152–1159.
14 A. Y. Mutlu, V. Kılıç, G. K. Özdemir, A. Bayram, N. Horzum and M. E. Solma, *Analyst*, 2017, **142**, 2434–2441.
15 L. Guo, J. A. Jackman, H. Yang, P. Chena, N. Cho and D. Kim, *Nano Today*, 2015, **10**, 213–239.
16 D. S. Rahman, S. Deb and S. K. Ghosh, *J. Phys. Chem. C*, 2015, **119**, 27145–27155.
17 N. Aissaoui, K. Moth-Poulsen, M. Käll, P. Johansson, L. M. Wilhelmsson and B. Albinsson, *Nanoscale*, 2017, **9**, 673–683.
18 A. Samanta, Y. Zhou, S. Zou, H. Yan and Y. Liu, *Nano Lett.*, 2014, **14**, 5052–5057.
19 A. B. Taylor and P. Zijlstra, *ACS Sens.*, 2017, **2**, 1103–1122.
20 N. Li, P. Zhao and D. Astruc, *Angew. Chem., Int. Ed.*, 2014, **53**, 1756–1789.
21 N. G. Bastus, J. Piella and V. Puntes, *Langmuir*, 2016, **32**, 290–300.
22 S. Biswas and P. Kumbhakar, *Appl. Phys. A*, 2018, **124**, 6–16.
23 Z. Yong, D. Y. Lei, C. H. Lam and Y. Wang, *Nanoscale Res. Lett.*, 2014, **9**, 187–193.
24 J. Yang, Y. Zhang, L. Zhang, H. Wang, J. Nie, Z. Qin, J. Li and W. Xiao, *Chem. Commun.*, 2017, **53**, 7477–7780.
25 S. Krishnamurthy, A. Esterle, N. C. Sharma and S. V. Sahi, *Nanoscale Res. Lett.*, 2014, **9**, 627–636.
26 N. D. Burrows, S. Harvey, F. A. Idesis and C. J. Murphy, *Langmuir*, 2017, **8**, 1891–1907.
27 H. Zhu, M. Chen, J. Yue, L. Liang, X. Jiang, *et al.*, *J. Nanopart. Res.*, 2017, **19**, 183–195.
28 S. E. Lohse and C. J. Murphy, *Chem. Mater.*, 2013, **25**, 1250–1261.
29 S. K. Meena, S. Celiksoy, P. Schäfer, A. Henkel, C. Sönnichsen and M. Sulpiz, *Phys. Chem. Chem. Phys.*, 2016, **18**, 13246–13254.
30 N. Almora-Barrios, G. Novell-Leruth, P. Whiting, M. Liz-MarzánL and N. López, *Nano Lett.*, 2014, **14**, 871–875.
31 J. Guo, M. J. Armstrong, C. M. O'Driscoll, J. D. Holmesb and K. Rahme, *RSC Adv.*, 2015, **5**, 17862–17871.
32 Y. Wu, Y. Gao and J. Du, *Talanta*, 2019, **197**, 599–604.
33 J. Li, P. Huang and F. Wu, *RSC Adv.*, 2017, **7**, 13426–13432.
34 A. Capocefalo, D. Mammucari, F. Brasili, C. Fasolato, F. Bordi, P. Postorino and F. Domenici, *Front. Chem.*, 2019, **7**, 413–424.
35 J. X. Dong, Z. F. Gao, Y. Zhang, B. L. Li, W. Zhang, J. L. Lei, N. B. Li and H. Q. Luo, *NPG Asia Mater.*, 2016, **8**, 335–345.
36 K. Bae, J. Lee, G. Kang, D. Yoo, C. Lee and K. Kim, *RSC Adv.*, 2015, **5**, 103052–103059.
37 B. Li, X. Li, Y. Dong, B. Wang, D. Li, Y. Shi and Y. Wu, *Anal. Chem.*, 2017, **89**, 10639–10643.
38 J. Schanda, *Colorimetery: Understanding the CIE System*, John Wiley & Sons, 2007.
39 M. M. Hawkeye and M. J. Brett, *RSC Adv.*, 2015, **5**, 103052–103059.
40 G. Niu, P. Zhang, W. Liu, M. Wang, H. Zhang, J. Wu, L. Zhang and P. Wang, *Anal. Chem.*, 2017, **89**(3), 1922–1929.
41 S. Singha, D. Kim, H. Seo, S. W. Choa and K. H. Ahn, *Chem. Soc. Rev.*, 2015, **44**, 4367–4399.
42 N. Manjubaashini, M. P. Kesavan, J. Rajesh and T. D. Thangadurai, *J. Photochem. Photobiol., B*, 2018, **183**, 374–384.
43 G. A. Jones and D. S. Bradshaw, *Front. Phys.*, 2019, **7**, 1–19.
44 E. Kohr, B. I. Karawdeniya, J. R. Dwyer, A. Gupta and W. B. Eule, *Phys. Chem. Chem. Phys.*, 2017, **19**, 27074–27080.
45 (*a*) R. Vogel, P. Meredith and M. D. Harvey, *Spectrochim. Acta, Part A*, 2004, **60**, 245–249; (*b*) C. On, E. K. Tanyi, E. Harrison and M. A. Noginov, *Opt. Mater. Express*, 2017, **7**, 4286–4295.
46 (*a*) Q. He, Y. Gao, L. Zhang, W. Bu, H. Chen, Y. Lib and J. Shi, *J. Mater. Chem.*, 2011, **21**, 15190–15192; (*b*) S. Monti, G. Barcaro, L. Sementa, V. Carravetta and H. Ågren, *RSC Adv.*, 2017, **7**, 49655–49663.
47 J. G. Xu and Z. B. Wang, *Fluorimetric Analysis Method*, Science Press, Beijing, 3rd edn, 2006, p. 65.
48 V. M. C. Würth, M. Kraft, M. B. A. J. Baeumner, U. Resch-Genger and T. Hirsch, *Anal. Chem.*, 2017, **899**, 4868–4874.
49 J. R. Lakowicz, *Principles of Fluorescence Spectroscopy*, Kluwer, New York, 2nd edn, 1999.
50 D. K. Sasmal, L. Pulido, S. Kasal and J. Huang, *Nanoscale*, 2016, **8**, 19928–19944.